

Unifying Plasticity in Ordered and Disordered Matter using Topological and Geometrical Descriptors

Xin Wang^{1,*}, Yang Xu^{1,2,*}, Jin Shang^{1,3}, Yi Xing¹, Jie Zhang^{1,3,†}

Yujie Wang^{1,4,5,‡}, Walter Kob^{4,6,§} and Matteo Baggioli^{1,2,7¶}

¹*School of Physics and Astronomy, Shanghai Jiao Tong University, Shanghai 200240, China*

²*Wilczek Quantum Center, Shanghai Jiao Tong University, Shanghai 200240, China*

³*Institute of Natural Sciences, Shanghai Jiao Tong University, Shanghai 200240, China*

⁴*School of Physics, Chengdu University of Technology, Chengdu, 610059, China*

⁵*State Key Laboratory of Geohazard Prevention and Geoenvironment Protection, Chengdu University of Technology, Chengdu, 610059, China*

⁶*Department of Physics, University of Montpellier and CNRS, 34095 Montpellier, France and*

⁷*Shanghai Research Center for Quantum Sciences, Shanghai 201315, China*

Identifying the regions responsible for plastic flow in amorphous solids remains an open problem, since structural disorder seems to prevent the direct application of concepts such as dislocations, topological defects that successfully describe irreversible deformations in crystalline systems. Here, we introduce fields of dislocation, disclination, and incompatibility densities, that reduce to the standard sources of plasticity in crystals and assess their predictive power in amorphous materials. We find that, in a simulated two-dimensional glass as well in two- and three-dimensional experimental granular systems, these fields exhibit strong spatial correlations with D_{\min}^2 , the standard measure used to locate plastic events under shear in disordered solids. Unlike D_{\min}^2 , these fields also allow to disentangle rotational and translational contributions to the plastic events, revealing that rotational defects becoming dominant in three dimensions. Our approach paves the way for a unified description of plasticity in crystalline and amorphous solids.

Introduction: When subjected to external loading, solids respond through a combination of reversible elastic deformations and irreversible plastic rearrangements, which involve local structural reorganization. In crystalline materials, plasticity is understood in terms of lattice defects, primarily dislocations [1, 2]. These are topological defects characterized by a discrete Burgers vector [3–5], and can experimentally be visualized by tracking atomic positions [6].

Within the continuum geometric framework developed by Kondo [7], Bilby [8], and Kröner [9], dislocations emerge as sources of torsion in an effective material geometry [10, 11], with the torsion tensor directly corresponding to the dislocation density [12, 13]. A closely related geometric and topological description applies to disclinations [10], defects associated with broken orientational order that play a central role in liquid crystals and also appear in crystalline solids, for instance in two-dimensional melting [14].

Plasticity is equally ubiquitous in amorphous materials, which lack long-range order and exhibit deformation across a wide range of length scales and levels of complexity [15]. In this case, however, the absence of translational order prevents a direct identification of plastic activity with topological defects such as dislocations, and precludes any obvious *a priori* characterization prior to deformation.

Building on Argon’s early work [16] on localized, irreversible atomic rearrangements, Falk and Langer introduced as a measure of plastic activity in amorphous solids D_{\min}^2 , a scalar quantity which quantifies local non-

affine displacements [17]. While the identified non-affine motion is often associated with plastic rearrangements, D_{\min}^2 remains a phenomenological and somewhat ad hoc measure, and is not in one-to-one correspondence with irreversible plastic events. Moreover, it is largely disconnected from the geometric and topological observables used to describe defects in crystals, reinforcing the view that the carriers of plasticity in amorphous and crystalline solids are fundamentally distinct. However, this distinction is likely artificial, since crystals with finite disorder can be expected to smoothly interpolate between ordered crystals and glasses.

In this work, we show that plastic rearrangements in amorphous solids can be formulated in terms of continuous fields that, in the crystalline limit, reduce to the standard descriptors of crystalline plasticity, namely the densities of topological defects and strain incompatibility. This establishes a unified description of plasticity across ordered and disordered solids and further reinforces the role of topological defects in amorphous matter [18].

Theory: In crystalline solids, the topological invariant associated with dislocations is the Burgers vector [19],

$$\vec{b} = \oint_{\mathcal{C}} d\vec{u}, \quad (1)$$

where \mathcal{C} is a closed loop and \vec{u} denotes the displacement field defined with respect to the ideal reference configuration. By Stokes’ theorem [10, 13], this line integral can be converted into a surface integral over any oriented

surface \mathcal{S} whose boundary is $\partial\mathcal{S} = \mathcal{C}$,

$$b_j(\vec{x}) = \oint_{\mathcal{C}} \partial_k u_j(\vec{x}) dx_k = \int_{\mathcal{S}} \epsilon_{ilk} \partial_l \partial_k u_j(\vec{x}) dS_i, \quad (2)$$

where dS_i is the oriented surface element normal to \mathcal{S} , ϵ_{ijk} is the three-dimensional Levi-Civita tensor, and the Einstein summation convention is implied. The result is independent of the specific choice of \mathcal{S} , provided that \mathcal{C} encloses the same defect content.

The integrand in Eq. (2) defines the (continuous, tensorial) Nye dislocation density,

$$\alpha_{ij}(\vec{x}) = \epsilon_{ilk} \partial_l \partial_k u_j(\vec{x}). \quad (3)$$

Similarly, the topological invariant associated with disclinations is the Frank vector [20],

$$\Omega_i = \oint_{\mathcal{C}} d\omega_i \quad \text{with} \quad \omega_i = \frac{1}{2} \epsilon_{ijk} \partial_j u_k. \quad (4)$$

Applying Stokes' theorem to Eq. (4), the corresponding disclination density is

$$\Theta_{ij}(\vec{x}) = \epsilon_{ilk} \partial_l \partial_k \omega_j(\vec{x}). \quad (5)$$

Importantly, within the geometric framework of mechanical deformations, the dislocation and disclination densities correspond, respectively, to the torsion and Riemann curvature tensors of the effective material metric. These definitions correctly reproduce the expected singularities associated with dislocations and disclinations in crystals (see Supplementary Information (SI) and [10] for explicit derivation).

Finally, one can define a tensorial defect density

$$\eta_{ij}(\vec{x}) = \epsilon_{ikl} \epsilon_{jmn} \partial_k \partial_m s_{ln}(\vec{x}), \quad (6)$$

where the strain tensor s_{ij} is related to the displacement field via $s_{ij} = \frac{1}{2}(\partial_i u_j + \partial_j u_i)$. The tensor η_{ij} , i.e., the double curl of the strain, is commonly referred to as the *Saint-Venant incompatibility tensor* (or *incompatibility density*) and characterizes local violations of the Saint-Venant compatibility condition [21]. A nonzero η_{ij} signals that the strain field cannot be derived from a single-valued displacement field, implying that the associated effective material metric cannot be globally embedded in Euclidean space. Physically, it quantifies the presence of internal (residual) stresses not induced by external loading, i.e., the stress is generated by an internal source, such as a defect.

We mention that, while dislocations and disclinations generate singularities in the incompatibility field, incompatibility is not restricted to such singular topological sources. Finite contributions can also arise from distributed eigenstrains or non-topological defects, such as vacancies or Stone-Wales defects, which locally distort the material without introducing discrete topological charges.

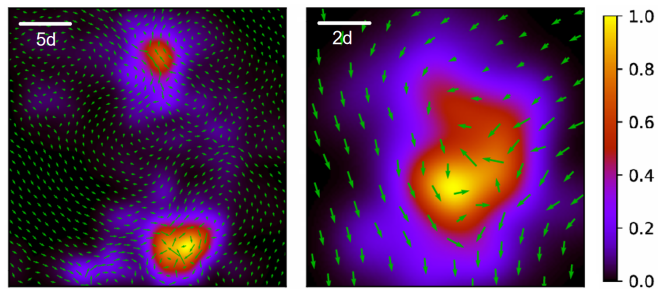


FIG. 1. **Defects in the displacement field.** Representative snapshots of the particle displacement field, overlaid on a heat map of the dislocation density $|\vec{\alpha}|$, normalized by its maximum value. **Left panel:** 2D simulated Lennard-Jones glass with strain step $\Delta\gamma = 0.5\%$. **Right panel:** Experimental 2D granular system with strain step $\Delta\gamma = 4.42\%$. In both panels, d denotes the particle diameter.

Note that in two dimensions [10], the dislocation density reduces to a vector field, $\alpha_i \equiv \alpha_{3i}$, while the disclination and incompatibility densities become scalar quantities, $\Theta \equiv \Theta_{33}$ and $\eta \equiv \eta_{33}$, with the index 3 denoting the out-of-plane direction perpendicular to the 2D system.

Turning to disordered solids, two remarks are in order. First, the absence of a unique, undeformed reference configuration prevents a straightforward definition of the displacement field from atomic positions. We therefore adopt a dynamical definition, $\vec{u} = \vec{x}(\gamma + \Delta\gamma) - \vec{x}(\gamma)$, evaluated over a small strain increment $\Delta\gamma$ under externally imposed shear γ . Additionally, in disordered solids, quantities such as the Burgers vector, which are topological and discrete in crystals, cease to represent true singularities and instead take continuous values, corresponding to what Kléman termed *continuous defects* [22] (see also Gilman [23, 24]). Consistent with this picture, continuous Burgers vectors have been shown to correlate with plastic activity in glasses [25–28].

Although displacement fields in amorphous systems lack true singularities, we retain the crystalline analogy and interpret α_{ij} , Θ_{ij} , and η_{ij} as the density fields of dislocations, disclinations, and incompatibility, respectively.

Crucially, our approach is not based on the topology of the eigenvector field, as explored in [29–36]. Instead, it focuses on the geometrical properties of the particle displacement field, which are used to construct the density fields for disclinations, dislocations, and incompatibility. Moreover, in contrast to the vortex-like defects identified in displacement fields in [37–41], we employ measures that naturally recover the classical notions of dislocations and disclinations in crystalline solids. Based on this continuity perspective, this construction resolves the ambiguities associated with defining topological defects in glasses.

To illustrate the meaning of the quantities introduced above, Fig. 1 presents two representative examples of the displacement field, together with the corresponding

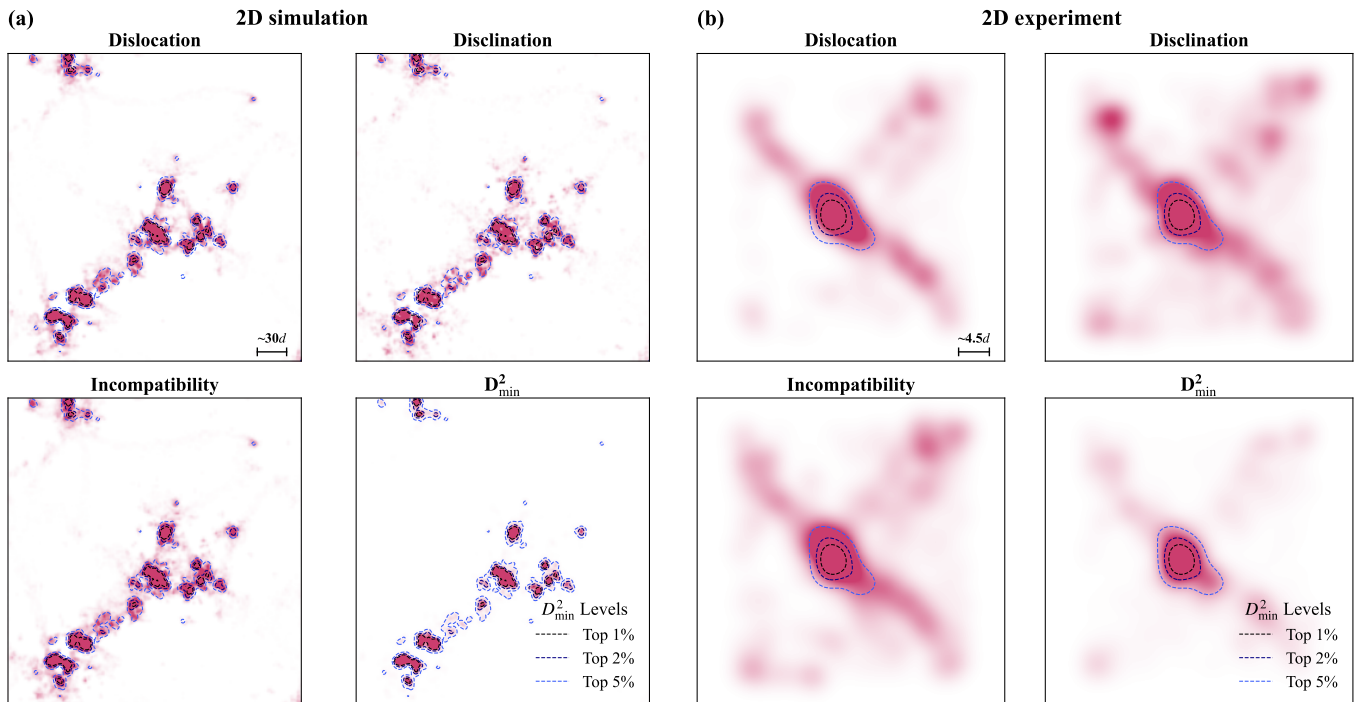


FIG. 2. **Comparison between defect densities and D_{\min}^2 in 2D.** Heat maps of the dislocation (3), disclination (5), and incompatibility (6) densities, together with D_{\min}^2 . For the dislocation density, we plot $|\vec{\alpha}|$. **(a)** 2D Lennard-Jones glass at strain $\gamma = 3.38\%$ with $\Delta\gamma = 0.02\%$. **(b)** 2D experimental granular system at $\gamma = 4.64\%$ with $\Delta\gamma = 0.113\%$. In both panels, the dashed contours indicate the top-percentile clusters of D_{\min}^2 . In both systems, d refers to the particle diameter.

heat map of the dislocation density (see SI for additional cases). As highlighted by the yellow–orange regions, the density accurately identifies incompatible zones, including local dislocation-like slip patterns (top spot in the left panel) and more complex geometrically incompatible structures (bottom spot in the left panel and the dominant signal in the right panel). By contrast, aside from minor numerical noise (blue regions), $|\vec{\alpha}|$ is small where the displacement field remains smooth. Importantly, regions characterized by large gradients yet a smooth underlying vector field do have a small value of the dislocation density, as they do not represent defects in this sense.

In SI, we include a comparison with vortex-like defects identified via the winding number, following the original construction applied to the eigenvector field in [29]. This analysis reveals a clear correlation between the location of the vortex defects and the spatial structure of the Nye dislocation density.

Continuous defect densities in amorphous solids: To investigate how well the defect density fields detect plasticity, we consider three systems: (i) A 2D binary Lennard–Jones glass with 10^4 particles, (ii) A 2D bidisperse frictional granular system consisting of 4065 photoelastic disks, and (iii) A monodisperse 3D frictional granular system made of 4200 3D-printed plastic spheres. The 2D systems (both numerical and experimental) are

driven by quasistatic pure shear applied through moving walls, while the 3D system is subjected to quasistatic simple shear. Further details on the systems, including the stress-strain curves, are provided in the *End Matter*.

Our analysis starts from the particle displacement field $u(\vec{x})$, computed at each strain step. To evaluate the densities defined in Eqs. (3)–(6), $u(\vec{x})$ is mapped onto a square (or cubic) lattice with spacing $a = d$, where d denotes the average particle diameter. We have verified that the results presented in the following are robust against variations in grid size, interpolation scheme, and even externally added noise. Additional details are provided in the SI.

Figure 2(a) shows, for the 2D Lennard–Jones system, the normalized density maps of the dislocation (3), disclination (5), and incompatibility (6) fields, together with the D_{\min}^2 , all measured at strain $\gamma = 3.38\%$ with $\Delta\gamma = 0.020\%$. Additional snapshots are provided in the SI. A striking visual similarity emerges among all four fields, particularly within the top-percentile clusters of D_{\min}^2 highlighted by dashed contours. This indicates that the three vector fields do carry similar information as D_{\min}^2 , and hence are useful indicators for plastic activity.

Panel (b) shows the same analysis for the 2D experimental system at $\gamma = 4.64\%$ with $\Delta\gamma = 0.113\%$. A clear correspondence between the four fields is again observed, although all fields appear noisier. We have checked that

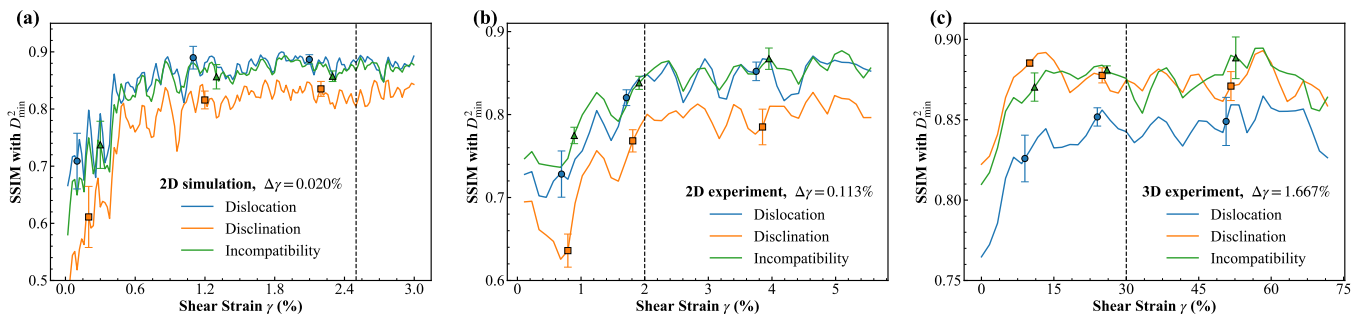


FIG. 3. **Quantifying the similarity between the fields.** Structural similarity index measure (SSIM) as a function of strain for three different systems: (a) 2D simulation, (b) 2D experiment, and (c) 3D experiment. The solid lines represent averages over three independent samples, while the symbols show representative data with corresponding error bars. Vertical dashed lines indicate the location of the yielding transition.

this increased noise is due to the smaller length scale shown in the experimental data, i.e., a similar magnitude of noise is also observed in the simulation data if one zooms in more (see SI). However, especially when focusing on the top-percentile regions, the agreement between the different measures remains strong.

Finally, we performed an analogous comparison for the 3D experimental system. Representative snapshots of the 3D density maps are shown in the *End Matter* and reveal again a pronounced degree of similarity among all quantities.

To provide a quantitative assessment of the similarity between the local map of D_{\min}^2 and the various defect densities introduced above, we consider the structural similarity index measure (SSIM) [42],

$$\text{SSIM}[X, Y] \equiv \frac{\text{Cov}(X, Y)}{\text{Std}(X)\text{Std}(Y)}. \quad (7)$$

The SSIM was obtained by mapping the fields onto a square/cubic lattice and calculating the covariance/variance of these mapped fields. Figure 3 shows the SSIM between the various physical fields and D_{\min}^2 as a function of shear strain for the different systems considered in this work.

For the 2D Lennard–Jones glass [panel (a)], the SSIM at small strains is approximately 0.5, 0.6, and 0.7 for the disclination, incompatibility, and dislocation densities, respectively. The correlation then increases rapidly and saturates around $\gamma^* \approx 0.5\%$, reaching values of about 0.85, 0.8, and 0.75, further confirming the strong correspondence between these quantities and D_{\min}^2 . Importantly, γ^* is consistently smaller than the yielding strain (vertical dashed line). This indicates that the high degree of similarity is not simply a consequence of large-scale plastic flow, but instead an intrinsic feature of these descriptors.

The weaker correlation at very small strain can be attributed to the dominance of elastic, nearly affine deformations, where both D_{\min}^2 and the defect densities are

weak and more susceptible to noise (see SI). We note that the curve for disclinations lies systematically below those for dislocations and incompatibility, suggesting that rotational defects play a subleading role for plasticity in two-dimensions.

Figure 3(b) presents the same similarity analysis for the 2D experimental data. Despite the very different nature of the interparticle potential and the presence of friction, the overall trend is consistent with the one of the simulations.

Finally, we present in Fig. 3(c) the analysis for the 3D granular system. Interestingly, we now find that the disclination density exhibits the strongest correlation with D_{\min}^2 , indicating a stronger role of angular defects over translational ones in three dimensions. This is consistent with previous findings highlighting disclination-like defects as topological signatures of plasticity in 3D sheared granular matter [43], as well as the role of vortex-like structures in granular systems [44].

The observed difference between two and three dimensions can be rationalized in terms of the interplay between geometric constraints and frictional interactions. In two dimensions, the limited rotational degrees of freedom strongly constrain local rearrangements, making plasticity predominantly mediated by translational defects such as local slips. In contrast, in three-dimensional systems, especially in the presence of friction, particles can undergo rotations about multiple axes, and tangential forces generate torques that provide an additional channel for stress relaxation. As a result, plastic events acquire a significant rotational component, leading to a more prominent role of rotational defects compared to translational ones.

To validate our analysis, we show in SI that an alternative similarity measure, the mean squared error (MSE), leads to consistent conclusions. Finally, in SI, we also examine the robustness of the correlations presented in Fig. 3 under both increasing strain interval $\Delta\gamma$ and the addition of external noise.

Outlook – In this work, considering both 2D and 3D simulated and experimental amorphous solids, we investigate the properties of density fields which in ordered materials reduce to standard indicators of plasticity – dislocation, disclination, and incompatibility densities. We show that these defect fields, computed in amorphous systems from the displacement field under deformation, exhibit a striking similarity to the standard non-affine measure D_{\min}^2 , and thus emerge as effective descriptors of plasticity even in disordered materials. These observations are in line with the geometric framework recently proposed by Moshe *et al.* [45–48] and the picture of *continuous defects* in the sense of Kléman [22].

This connection permits a unified description of plasticity across ordered and disordered materials: the fields that localize the discrete defects in crystals become in amorphous systems smooth quantities that signal the presence of enhanced plasticity. These fields are directly linked to the density of topological defects or the strength of incompatibility, making them valuable for describing plasticity even in the absence of well-defined underlying singularities—unlike other approaches based on vortices, e.g., [29, 31, 33–35, 37–41].

Additionally, the ability of these fields to distinguish between rotational and translational defects is particularly valuable, as it provides deeper insight into the nature of plastic events—something D_{\min}^2 cannot capture. This capability has already revealed a key difference between plasticity in two and three dimensions, where the roles of translational and rotational defects are reversed.

We also note that applying the same methods to the eigenvector fields of vibrational modes in the unperturbed configuration has been found to provide a robust predictor of plastic activity under deformation [36], i.e., this method is not only applicable as a purely *a posteriori* characterization.

Finally, from a theoretical perspective, it would be interesting to establish a more direct connection between these densities and the geometric charges introduced by Moshe *et al.* [45–48], as such a link could provide a clearer understanding of how defects relate to the anomalous elastic behavior observed in amorphous materials.

Acknowledgments – We thank M. Falk, P. Harrowell, M. Moshe, G. Szamel, C. Du, A. Zacccone, I. Regev, Z. Wu, A. Bera, L. Huang, Y. Wang and A. Liu for several useful discussions on this topic. MB acknowledges the support of the Shanghai Municipal Science and Technology Major Project (Grant No.2019SHZDZX01) and the support of the sponsorship from the Yangyang Development Fund. JS and JZ acknowledge the support of the NSFC (No.11974238, No.12274291 and No.12534008) and the Shanghai Municipal Education Commission Innovation Program under No. 2021-01-07-00-02-E00138. JS and JZ also acknowledge the support from the SJTU Student Innovation Center. XW, YX and YW are supported by the National Natural Science Foundation of

China (No. 12274292).

* These authors contributed equally to this work.

† jiezhang2012@sjtu.edu.cn

‡ yujiewang@sjtu.edu.cn

§ walter.kob@umontpellier.fr

¶ b.matteo@sjtu.edu.cn

- [1] E. Schmid and W. Boas, *Plasticity of Crystals: With Special Reference to Metals* (Chapman & Hall, 1968).
- [2] A. Sutton, *Physics of Elasticity and Crystal Defects*, Oxford Series on Materials Modelling (OUP Oxford, 2020).
- [3] J. V. Selinger, *Introduction to topological defects and solitons: in liquid crystals, magnets, and related materials*, Lecture Notes in Physics, Vol. 1032 (Springer, Cham, 2024) pp. XIII, 213 pages : illustrations.
- [4] S. Fumeron and B. Berche, *The European Physical Journal Special Topics* **232**, 1813 (2023).
- [5] P. Anderson, J. Hirth, and J. Lothe, *Theory of Dislocations* (Cambridge University Press, 2017).
- [6] C. L. Jia, A. Thust, and K. Urban, *Phys. Rev. Lett.* **95**, 225506 (2005).
- [7] K. Kazuo, *International Journal of Engineering Science* **2**, 219 (1964).
- [8] B. A. Bilby, R. Bullough, and E. Smith, *Proceedings of the Royal Society of London. Series A. Mathematical and Physical Sciences* **231**, 263 (1955).
- [9] E. Kröner, *Arch. Rat. Mech. Anal* **4**, 273 (1960).
- [10] H. Kleinert, *Gauge Fields in Condensed Matter*, Gauge Fields in Condensed Matter No. v. 2 (World Scientific, Singapore and Teaneck, N.J., 1989).
- [11] R. Kupferman, M. Moshe, and J. P. Solomon, *Archive for Rational Mechanics and Analysis* **216**, 1009 (2015).
- [12] E. Kröner, in *Physics of Defects*, Les Houches Summer School Proceedings, Vol. 35, edited by R. Balian, M. Kléman, and J.-P. Poirier (North-Holland, Amsterdam, 1981) pp. 215–315.
- [13] J. Nye, *Acta Metallurgica* **1**, 153 (1953).
- [14] J. M. Kosterlitz, *Rev. Mod. Phys.* **89**, 040501 (2017).
- [15] L. Berthier, G. Biroli, L. Manning, and F. Zamponi, *Nature Reviews Physics* (2025), 10.1038/s42254-025-00833-5.
- [16] A. Argon, *Acta Metallurgica* **27**, 47 (1979).
- [17] M. L. Falk and J. S. Langer, *Phys. Rev. E* **57**, 7192 (1998).
- [18] M. Baggioli, M. L. Falk, and W. Kob, *arXiv preprint arXiv:2604.07061* (2026).
- [19] F. C. Frank, *physica status solidi (a)* **105**, K21 (1988).
- [20] R. deWit, *Journal of Research of the National Bureau of Standards. Section A, Physics and Chemistry* **77A**, 49 (1973).
- [21] A. E. H. Love, *A Treatise on the Mathematical Theory of Elasticity* (Cambridge University Press, Cambridge, 1892) reprinted by Dover Publications, 1944.
- [22] M. Kleman and J. Friedel, *Rev. Mod. Phys.* **80**, 61 (2008).
- [23] J. Gilman, *Journal of Applied Physics* **44**, 675 (1973).
- [24] J. J. Gilman, *Journal of applied Physics* **46**, 1625 (1975).
- [25] M. Baggioli, M. Landry, and A. Zacccone, *Phys. Rev. E* **105**, 024602 (2022).
- [26] M. Baggioli, I. Kriuchevskiy, T. W. Sirk, and A. Zacccone, *Phys. Rev. Lett.* **127**, 015501 (2021).

- [27] A. C. Y. Liu, H. Pham, A. Bera, T. C. Petersen, T. W. Sirk, S. T. Mudie, R. F. Tabor, J. Nunez-Iglesias, A. Zaccone, and M. Baggioli, *Acta Crystallographica Section A* **82** (2026), 10.1107/S2053273325009775.
- [28] A. Bera, I. Regev, A. Zaccone, and M. Baggioli, arXiv preprint arXiv:2505.23069 (2025).
- [29] Z. W. Wu, Y. Chen, W.-H. Wang, W. Kob, and L. Xu, *Nat. Commun* **14**, 2955 (2023).
- [30] M. Baggioli, *Nature Communications* **14**, 2956 (2023).
- [31] V. Vaibhav, A. Bera, A. C. Y. Liu, M. Baggioli, P. Keim, and A. Zaccone, *Nature Communications* **16**, 55 (2025).
- [32] L.-Z. Huang, Y.-J. Wang, M.-Q. Jiang, and M. Baggioli, *Journal of the Mechanics and Physics of Solids* **204**, 106274 (2025).
- [33] A. Bera, A. Zaccone, and M. Baggioli, *Nature Communications* **16**, 5990 (2025).
- [34] Z. W. Wu, J.-L. Barrat, and W. Kob, *Nature Communications* (2025), 10.1038/s41467-025-66923-1.
- [35] E. A. Bedolla-Montiel and M. Dijkstra, “Striking similarities in dynamics and vibrations of 2d quasicrystals and supercooled liquids,” (2025), arXiv:2508.18856 [cond-mat.soft].
- [36] L.-Z. Huang, X. Yang, M.-Q. Jiang, Y.-J. Wang, and M. Baggioli, “A geometric approach to predicting plasticity in disordered solids,” (2025), arXiv:2512.12668 [cond-mat.soft].
- [37] A. Bera, M. Baggioli, T. C. Petersen, T. W. Sirk, A. C. Y. Liu, and A. Zaccone, *PNAS Nexus* **3**, pgae315 (2024).
- [38] P. Desmarchelier, S. Fajardo, and M. L. Falk, *Phys. Rev. E* **109**, L053002 (2024).
- [39] H. Rösner, A. Bera, and A. Zaccone, *Phys. Rev. B* **110**, 014107 (2024).
- [40] X. Wang, J. Shang, Y. Wang, J. Zhang, and M. Baggioli, arXiv preprint arXiv:2507.03771 (2025).
- [41] A. Bera, D. Majumdar, T. W. Sirk, I. Regev, and A. Zaccone, arXiv preprint arXiv:2507.09250 (2025).
- [42] Z. Wang and A. C. Bovik, *Modern Image Quality Assessment* (Morgan & Claypool, 2006).
- [43] Y. Cao, J. Li, B. Kou, C. Xia, Z. Li, R. Chen, H. Xie, T. Xiao, W. Kob, L. Hong, J. Zhang, and Y. Wang, *Nature Communications* **9**, 2911 (2018).
- [44] A. Tordesillas, S. Pucilowski, Q. Lin, J. F. Peters, and R. P. Behringer, *Journal of the Mechanics and Physics of Solids* **90**, 215 (2016).
- [45] M. Moshe, I. Levin, H. Aharoni, R. Kupferman, and E. Sharon, *Proceedings of the National Academy of Sciences* **112**, 10873 (2015).
- [46] N. S. Livne, A. Schiller, and M. Moshe, *Phys. Rev. E* **107**, 055004 (2023).
- [47] B. P. Bhowmik, M. Moshe, and I. Procaccia, *Phys. Rev. E* **105**, L043001 (2022).
- [48] A. Kumar and I. Procaccia, *Europhysics Letters* **145**, 26002 (2024).
- [49] R. Brüning, D. A. St-Onge, S. Patterson, and W. Kob, *Journal of Physics: Condensed Matter* **21**, 035117 (2008).
- [50] Y. Wang, J. Shang, Y. Jin, and J. Zhang, *Proceedings of the National Academy of Sciences* **119**, e2204879119 (2022).
- [51] Y. Wang, J. Shang, Y. Wang, and J. Zhang, *Physical Review Research* **3**, 043053 (2021).
- [52] Y. Xing, Y. Yuan, H. Yuan, S. Zhang, Z. Zeng, X. Zheng, C. Xia, and Y. Wang, *Nature Physics* **20**, 646 (2024).

END MATTER

Appendix A: Systems –

Simulated 2D Lennard-Jones glass: The system is a binary Lennard–Jones model that is not prone to crystallization [49]. The interaction between particles of species $\alpha, \beta \in \{A, B\}$ is given by

$$V_{\alpha\beta}(r) = 4\epsilon_{\alpha\beta} \left[\left(\frac{d_{\alpha\beta}}{r} \right)^{12} - \left(\frac{d_{\alpha\beta}}{r} \right)^6 \right], \quad (8)$$

with $\epsilon_{AA} = 1.0$, $\epsilon_{AB} = 1.5$, $\epsilon_{BB} = 0.5$ and $d_{AA} = 1.0$, $d_{AB} = 0.8$, $d_{BB} = 0.88$. We use $N = 10^5$ particles with a composition of $N_A : N_B = 65:35$. The system is initialized in a square box with periodic boundary conditions. Four confining walls are generated by exploiting the periodic boundary conditions and freezing a particle layer of width $3d_{AA}$ around the central simulation box.

To obtain an equilibrated, low-temperature glass, the system is quenched to temperature $T = 10^{-7}$ in the NVT ensemble for 10^6 steps. The box size was 280.3 which corresponds to a particle density of 1.27 . Subsequently, one pair of walls is driven at constant velocity $|v_x| \approx 10^{-3}$ to impose a shear rate $\dot{\gamma} \approx 10^{-5}$, while the opposite walls move to preserve the area of the bulk region, mirroring the experimental protocol of pure shear. The resulting stress–strain response is shown in Fig. 4(a). The inset illustrates the pure shear deformation applied. The yielding transition is located at $\gamma \approx 2.5\%$. In the SSIM analysis, we excluded approximately six particle layers near the walls and focused on the bulk region.

–Experimental 2D granular matter system: The 2D granular assembly consists of 2710 small and 1355 large photoelastic disks with diameters $d_s = 10$ mm and $d_l = 14$ mm. The disks rest on a horizontal glass plate inside a rectangular region bounded by two pairs of independently movable smooth walls, enabling area-preserving pure shear. Experimental data were

recorded using a 2×2 array of high-resolution cameras (10 pixels/mm) mounted above the system. Additional details on the setup can be found in Refs. [50, 51]. The stress–strain curve for this system is shown in Fig. 4(b). The inset depicts the applied pure shear deformation. The yielding transition is located at $\gamma \approx 2\%$. In the experiment, the uncertainty in particle position determination is on the order of $1/100d$. In the SSIM analysis, we excluded approximately six particle layers near the walls and focused on the bulk region.

–Experimental 3D granular matter system: The 3D packing consists of monodisperse, 3D-printed plastic spheres of diameter $d = 6$ mm. The shear cell has dimensions $24d$ times $24d$ time $24d$ and is sheared in the x -direction. More than 4200 particles located at least $2.5d$ away from the shear cell boundaries were analyzed. The packing was first cyclically sheared under constant pressure to reach a reproducible initial volume fraction, and then sheared unidirectionally in uniform strain increments until the sample attained a maximum in volume, i.e., it has reached the state of random loose packing. X-ray tomography was used to capture the 3D structure at each strain step, while a force sensor simultaneously measured the shear force. Further experimental details are provided in Ref. [52]. The resulting stress–strain curve is shown in Fig. 4(c). The inset illustrates the simple shear deformation applied. The yielding transition is located at $\gamma \approx 30\%$. In the experiment, the uncertainty in particle position determination is on the order of $10^{-3}d$. In the SSIM analysis, we excluded approximately four particle layers near the walls and focused on the bulk region.

Appendix B: Density fields for the three dimensional system – In Figure 5, we present an example of the comparison between the spatial distribution of the dislocation (3), disclination (5), incompatibility (6) densities and D_{\min}^2 from the 3D experimental data. For each tensorial density, we plot its norm. The similarity among the four measures is evident.

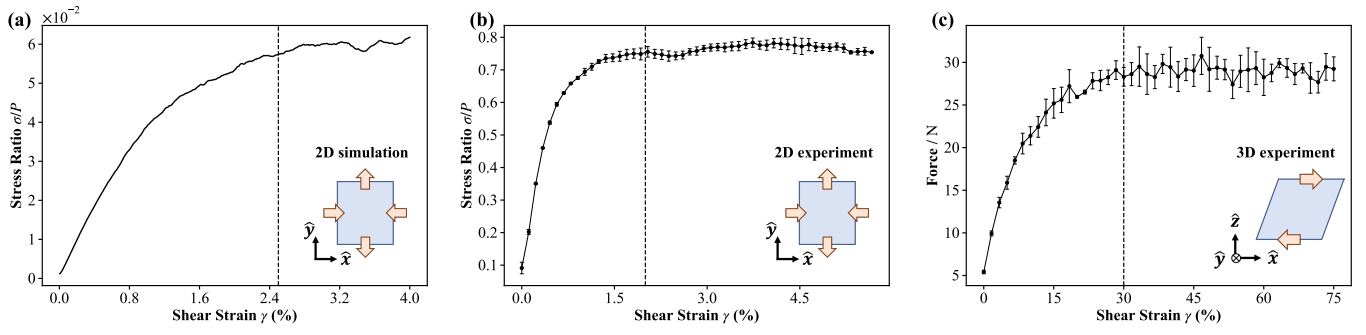


FIG. 4. **Mechanical properties under shear deformation.** Stress ratio and force as a function of strain γ . (a) 2D simulation, (b) 2D experiment, and (c) 3D experiment. The insets show a schematic cartoon of the applied shear deformation for each case. In panels (a) and (b), σ denotes the shear stress and P the pressure. Vertical lines indicate the yielding strain.

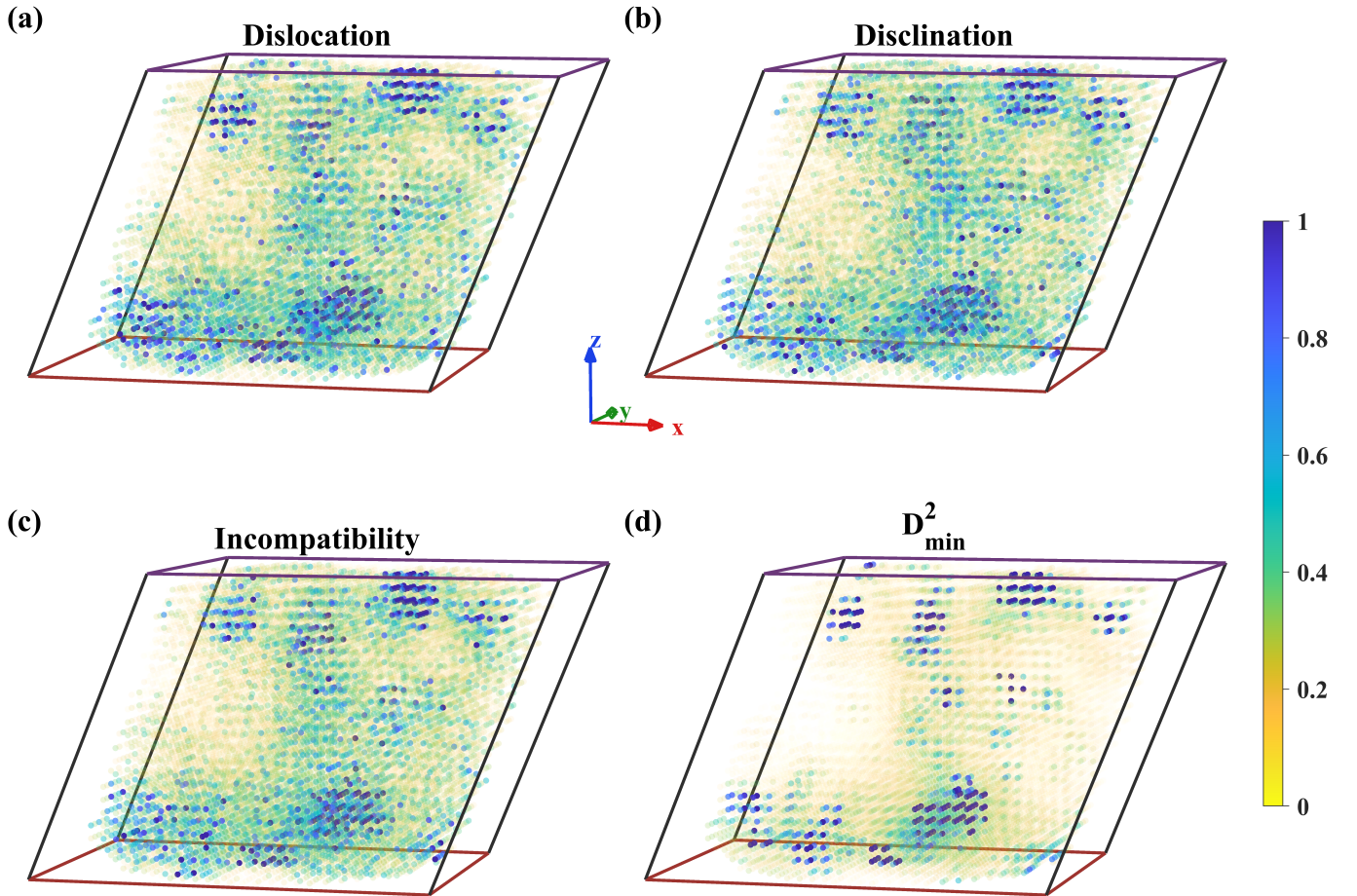


FIG. 5. **Comparison between defect densities and D_{\min}^2 in 3D.** Normalized norm of the (a) dislocation, (b) disclination, (c) incompatibility densities and (d) D_{\min}^2 in 3D experimental granular system with $\gamma = 38.33\%$. The samples are sheared in the x -direction.

Supplementary Information for “Unifying Plasticity in Ordered and Disordered Matter using Topological and Geometrical Descriptors”

Xin Wang, Yang Xu, Jin Shang, Yi Xing, Jie Zhang, Yujie Wang, Walter Kob, Matteo Baggioli

In this Supplementary Information, we provide further details about the computational methods used in this study and the analysis of the continuous densities.

CONTENTS

SI1: Computational methods	9
SI2: Robustness of the dislocation density under external artificial noise	9
SI3: Defect densities for different strain intervals	11
SI4: Mean Squared Error (MSE) similarity analysis	11
SI5: Structural Similarity Index Measure (SSIM) between density fields	12
SI6: Effect of visualization scale on apparent blur in Figure 2 in main text	13
SI7: Continuous defect densities in the 2D Lennard-Jones simulated glass at low strain	14
SI8: Demonstration of the robustness of plastic defect structures with respect to grid size, interpolation scheme and grid positioning	14
SI9: Extended analysis on continuous defect densities in 2D experimental granular systems	15
SI10: Stability of the similarity analysis against grid size and interpolation scheme	16
SI11: Defects captured by continuous densities and comparison to vortex-like defects	16
SI12: Ideal topological defects and their singular contribution to the continuous defect densities	18

SI1: Computational methods

Since the particle displacements are associated with the positions of the particle and the latter are distributed in space in a disordered manner, this field is defined only at discrete points. To compute spatial derivatives one needs, however, a continuous displacement field. Since derivatives cannot be evaluated directly on irregularly spaced data points, we map the displacement field onto a regular grid and then compute derivatives using central finite differences.

First, we apply linear interpolation to obtain displacement values on a grid with spacing a . Thus for the 2D systems we have

$$u(x, y) \longrightarrow u(i, j), \quad (\text{S1})$$

where i and j give the position on the lattice. The displacement field on the lattice has the same information as the particle displacement. As demonstrated in Fig. S1, the main features of the different fields do not depend in a significant manner on the interpolation procedure, i.e., this approach allows to make a robust analysis of their characteristics.

We then approximate the spatial derivatives by central differences:

$$\frac{\partial u}{\partial x} = \lim_{\Delta x \rightarrow 0} \frac{u(x + \frac{1}{2}\Delta x, y) - u(x - \frac{1}{2}\Delta x, y)}{\Delta x} \longrightarrow \frac{\partial u}{\partial x} = \frac{u(i+1, j) - u(i-1, j)}{2}, \quad (\text{S2})$$

$$\frac{\partial u}{\partial y} = \lim_{\Delta y \rightarrow 0} \frac{u(x, y + \frac{1}{2}\Delta y) - u(x, y - \frac{1}{2}\Delta y)}{\Delta y} \longrightarrow \frac{\partial u}{\partial y} = \frac{u(i, j+1) - u(i, j-1)}{2}. \quad (\text{S3})$$

Higher order derivatives are obtained in the same manner. Finally, we apply a Gaussian smoothing with width of $1.5d$ (with d the particle diameter) to reduce numerical noise in the resulting fields for all systems.

SI2: Robustness of the dislocation density under external artificial noise

It is important to verify to what extent the various vector fields studied in the present work are affected by noise, since thermal fluctuations and experimental errors will prevent to have a perfect knowledge of these fields. To study these effects, we have added artificial noise to the displacement field:

$$v_{\text{noise},i}(\vec{x}) = v_i(\vec{x}) [1 + R \xi_i(\vec{x})], \quad i = x, y, z, \quad (\text{S4})$$

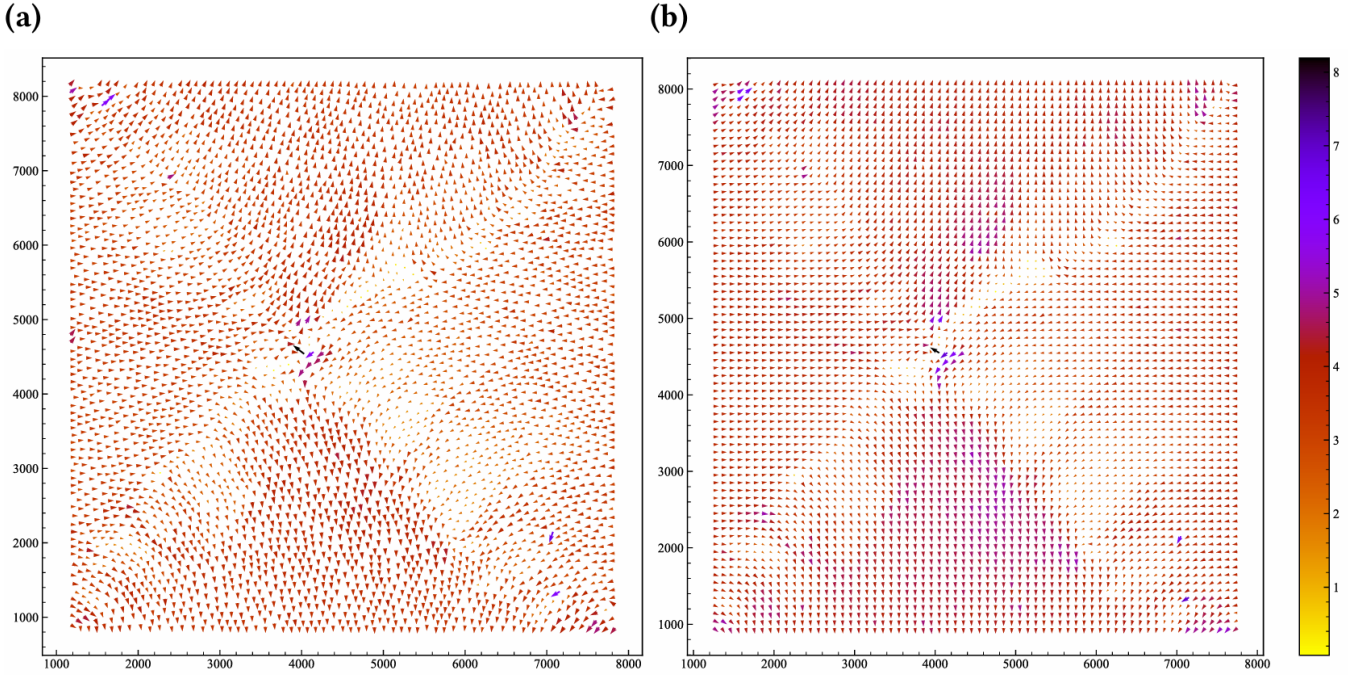


FIG. S1. Two-dimensional experimental system: **(a)** Displacement vectors defined at particle positions. **(b)** Continuous displacement field obtained by interpolation onto a grid with spacing $a = 1.0 d_s$ with d_s the diameter of the small particles.

where each component of the random vector $\vec{\xi}$ follows a Gaussian distribution with zero mean and unit standard deviation, and R is the amplitude of the noise. The influence of this noise on the structural similarity index measure (SSIM) for the case of the 2D Lennard-Jones system is presented in Fig. S2, for different noise amplitudes R .

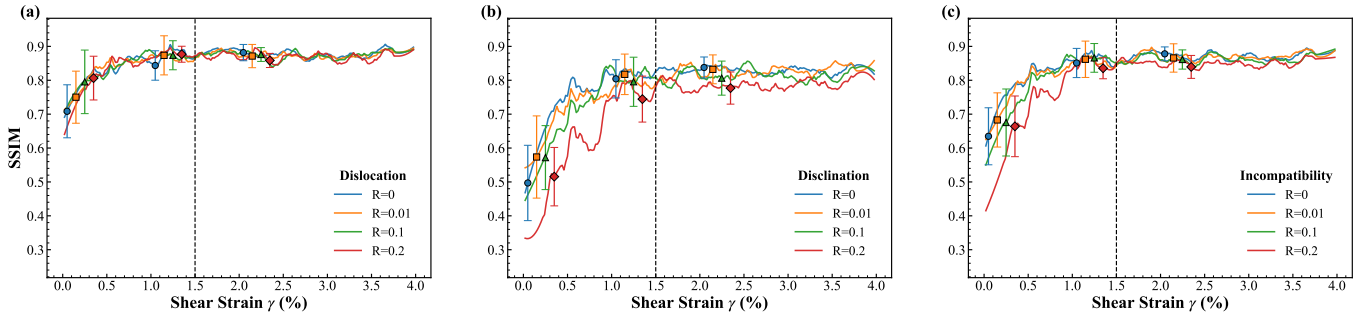


FIG. S2. Structural Similarity Index Measure (SSIM) for increasing artificial noise in the displacement field (see Eq. (S4)) for the 2D Lennard-Jones simulation. Panels (a)–(c) show, respectively, the SSIM between the dislocation, disclination, and incompatibility densities and D_{\min}^2 . The vertical dashed line indicates the yielding strain of the simulated system.

As the noise amplitude increases, the similarity between the disclination and incompatibility densities and D_{\min}^2 decreases, particularly in the pre-yield regime ($\gamma < 1\%$). On the other hand, the dislocation density consistently retains a higher similarity compared to the others. This indicates that the dislocation density exhibits superior robustness against external perturbations.

In Fig. S3, we present the spatial structure of the dislocation density for various levels of noise. One recognizes that this structure is indeed not affected significantly when the noise level is increased.

We have repeated the same type of perturbation for the 2D experimental and 3D experimental systems and in Fig. S4 and S5, we present the corresponding results. As in the simulations, the dislocation density remains a robust indicator except at the largest noise level ($R = 0.2$), whereas the other two densities are more strongly affected by artificial noise, showing a noticeable drop in SSIM with D_{\min}^2 . This confirms the superior stability of the dislocation density as a measure of plasticity in for all systems.

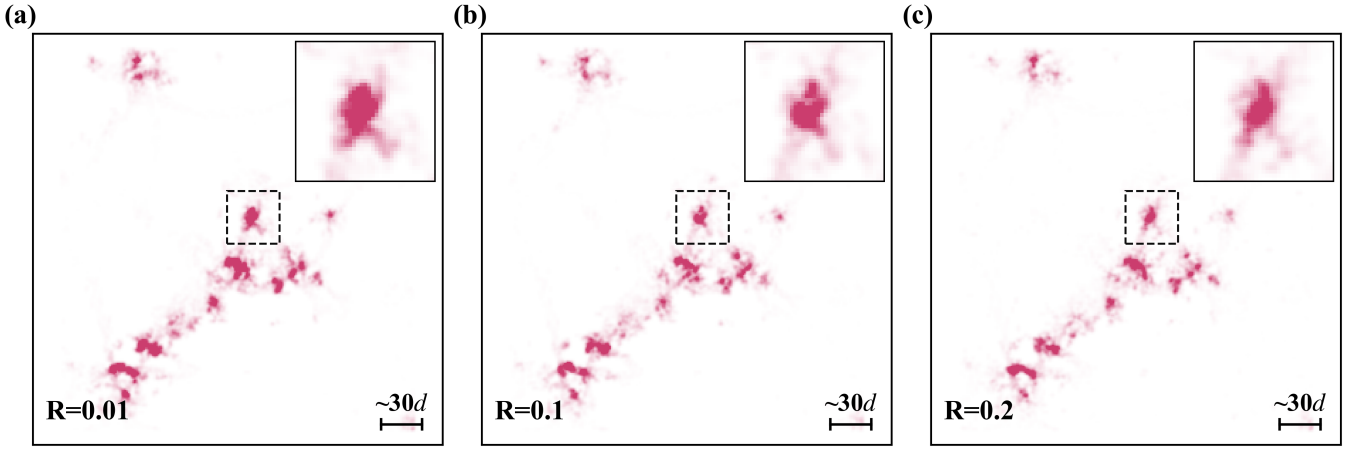


FIG. S3. Snapshots of the dislocation density for the 2D simulation at $\gamma = 3.84\%$ with added noise levels of 0.01, 0.1, and 0.2, corresponding to panels (a)–(c), respectively. In each panel, the inset displays a magnified view of the dashed region in the main plot.

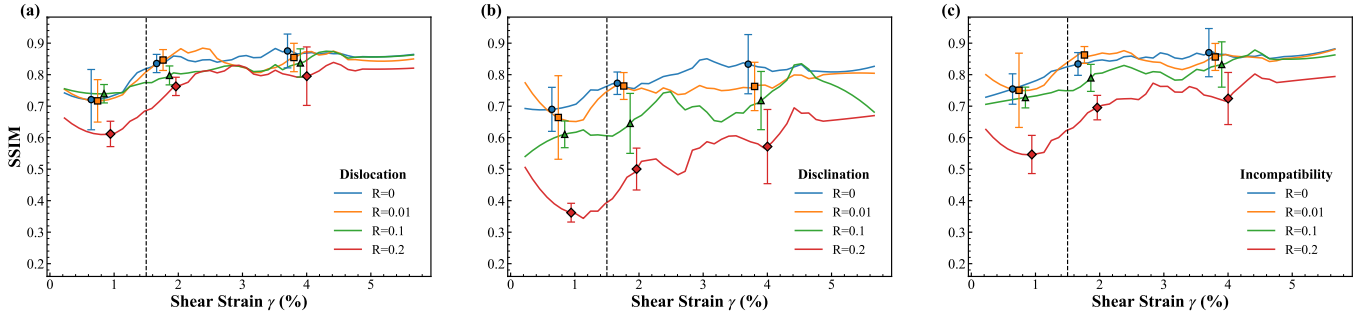


FIG. S4. Structural Similarity Index Measure (SSIM) for increasing artificial noise in the displacement field (see Eq. (S4)) for the 2D experimental data. Panels (a)–(c) show, respectively, the SSIM between the dislocation, disclination, and incompatibility densities and D_{\min}^2 . The vertical dashed line indicates the yielding strain of the experimental system.

SI3: Defect densities for different strain intervals

The details of the dislocation, disclination, and incompatibility fields will depend on the strain increment used to calculate the displacement field. To assess the robustness of the analysis presented in the main text with respect to the choice of this strain interval $\Delta\gamma$, we examine two additional values, $\Delta\gamma = 0.1\%$ and 0.2% , using the 2D Lennard-Jones simulation data. The resulting values for the SSIM are shown in Fig. S6, where we include also the data from the main text, i.e., $\Delta\gamma = 0.02\%$.

Overall, the correlation between the defect density fields and D_{\min}^2 remains robust, particularly above yielding (indicated by the vertical dashed black line). Interestingly, increasing the strain interval leads to a gradual deterioration of the correlation between D_{\min}^2 and both the disclination and incompatibility densities for $\gamma \lesssim 1\%$. In contrast, the correlation between the dislocation density and D_{\min}^2 appears largely insensitive to variations in $\Delta\gamma$.

SI4: Mean Squared Error similarity analysis

In the main text we have used the SSIM to quantify the similarity between the various fields. Another possibility to do this is via the Mean Squared Error (MSE) analysis. Given two fields X_i and Y_i whose values are normalized between 0 and 1, where i indicates the position on the lattice, the MSE is defined as

$$\text{MSE} = \frac{1}{n} \sum_{i=1}^n (X_i - Y_i)^2, \quad (\text{S5})$$

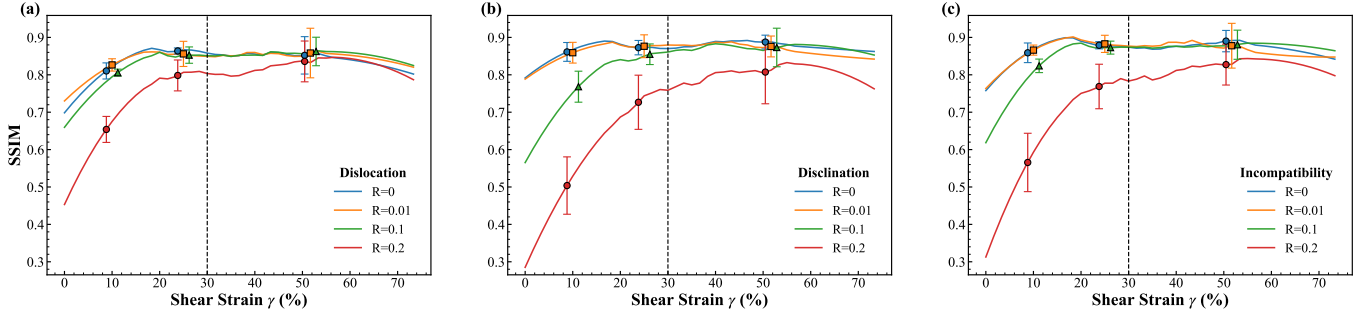


FIG. S5. Structural Similarity Index Measure (SSIM) for increasing artificial noise in the displacement field (see Eq. (S4)) for the 3D experimental data. Panels (a)–(c) show, respectively, the SSIM between the dislocation, disclination, and incompatibility densities and D_{\min}^2 . The vertical dashed line indicates the yielding strain of the experimental system.

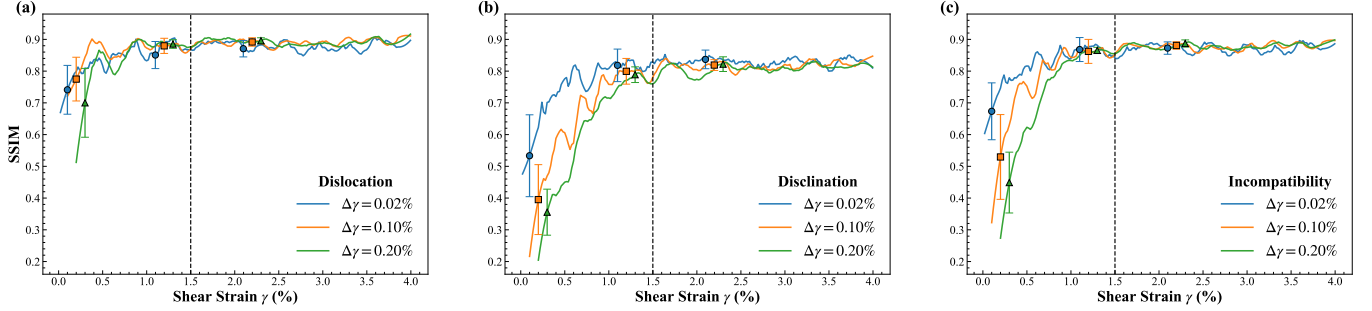


FIG. S6. Structural Similarity Index Measure (SSIM) for different strain intervals, $\Delta\gamma = 0.02\%$, 0.10% , and 0.20% , between D_{\min}^2 and (a) the dislocation, (b) disclination, and (c) incompatibility density fields. These data refer to the 2D simulations. The vertical dashed lines indicate the yielding strain for each system.

where n is the number of grid points. A small MSE value indicates thus a good match between the two fields. Figure S7 shows the MSE between the various density fields and D_{\min}^2 . In all cases, the MSE remains very small, confirming the high degree of similarity between these quantities reported in the main text. One does hence conclude that the documented ability of the three fields to predict the location of plastic activity is not due to the choice of the descriptor.

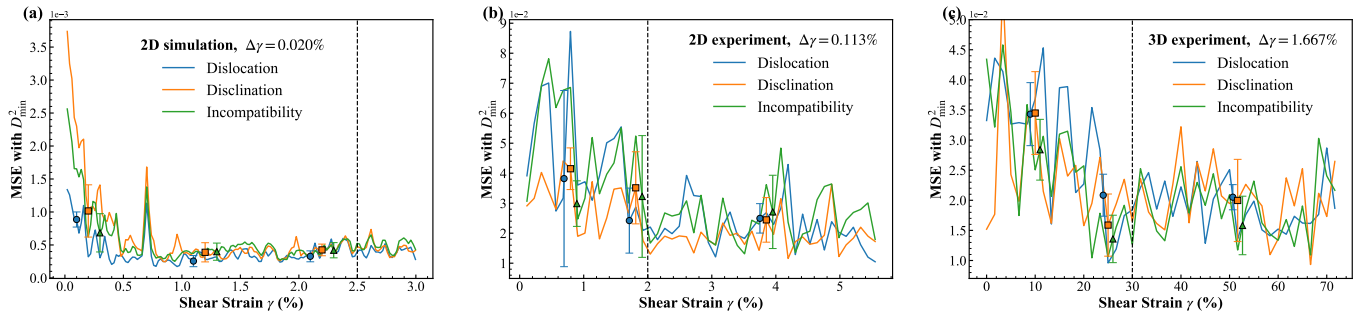


FIG. S7. Mean Squared Error (MSE) as a function of strain for (a) 2D simulation, (b) 2D experiment and (c) 3D experiment.

SI5: Structural Similarity Index Measure between density fields

Using the definition of the Structural Similarity Index Measure (SSIM) introduced in Eq. (7) of the main text, one can also measure the correlation between the different density fields. The results for the 2D Lennard-Jones simulation are reported in Fig. S8(a).

For strains above $\gamma^* \approx 0.5\%$, both the dislocation–incompatibility and disclination–incompatibility correlations are very high, reaching values of approximately 95%. In contrast, within the quasi-elastic linear regime ($\gamma^* < 0.5\%$), the correlation between the disclination and incompatibility fields appears slightly stronger than the others. This indicates that at small strain the incompatibility is mainly of disclination nature, i.e., the particles start to rotate against each other. Qualitatively the same results are obtained by monitoring the MSE, see panel (b).

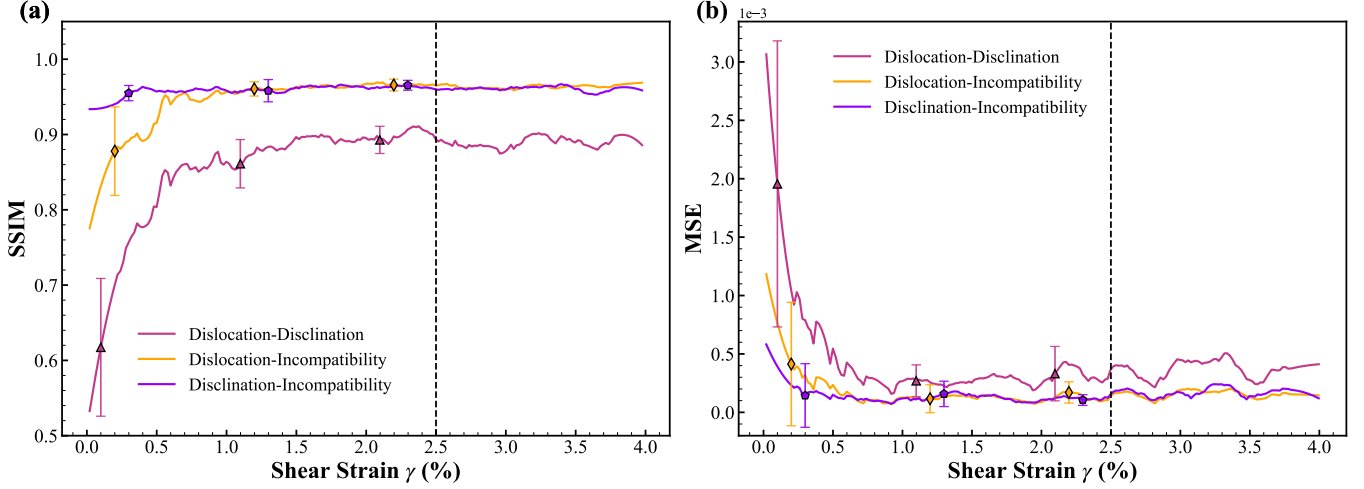


FIG. S8. Pairwise similarity between continuous fields for the 2D simulation data. (a) Structural Similarity Index Measure (SSIM) and (b) Mean Squared Error (MSE) for the dislocation, disclination, and incompatibility densities. The vertical dashed line indicates the yielding strain.

SI6: Effect of visualization scale on apparent blur in Figure 2 in main text

In the context of Fig. (2) in the main text, we noted that the experimental data appear more blurred than the simulation results. We attributed this difference to the disparity in sample size. To verify this, we rescaled and cropped the simulation data to match the magnification and image dimensions of the experimental data (see Fig. S9). The resulting images display a comparable level of blur, indicating that the difference in sharpness arises from visualization effects rather than any underlying physical discrepancy between the experimental and simulated systems.

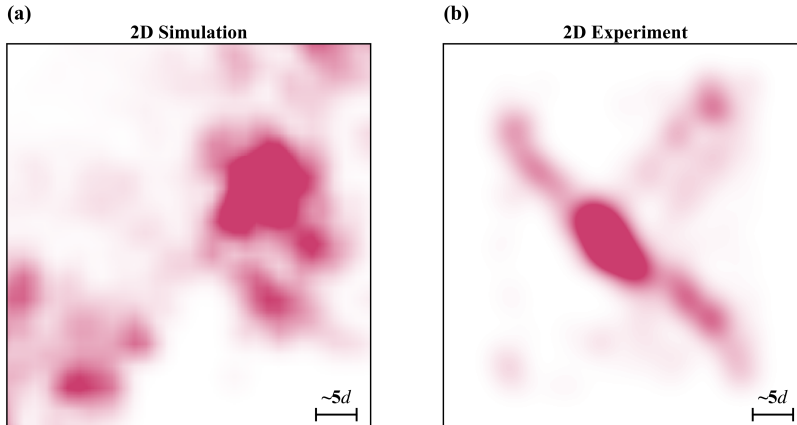


FIG. S9. (a) Magnified view of the defect density maps for the 2D simulations shown in Fig. (2)(a) of the main text (enlarged by a factor of $30/4$). This rescaling places the sample, in units of the particle diameter, on a length scale comparable to that of the 2D experimental system (see scale bar). (b) Experimental 2D data displayed at the same length scale. The simulation and experimental images exhibit a comparable level of blur in the density field.

SI7: Continuous defect densities in the 2D Lennard-Jones simulated glass at low strain

In the main text (Fig. (2)) we present a direct comparison between the defect densities and D_{\min}^2 at a relatively large strain, $\gamma = 3.38\%$. For completeness, Fig. S10 presents four additional comparisons between D_{\min}^2 and the incompatibility density η at low strain. Panels (a)–(c) correspond to $\gamma \lesssim 0.2\%$, where the SSIM with D_{\min}^2 (see Fig. (3) in the main text) remains moderate (in the range 50%–80%). In this regime, the response is predominantly elastic, with only sparse plastic rearrangements of small amplitude. The non-affine measure D_{\min}^2 is noisy and spatially delocalized. While a clear visual similarity between η and D_{\min}^2 is already evident, the quantitative agreement is limited by the substantial background noise.

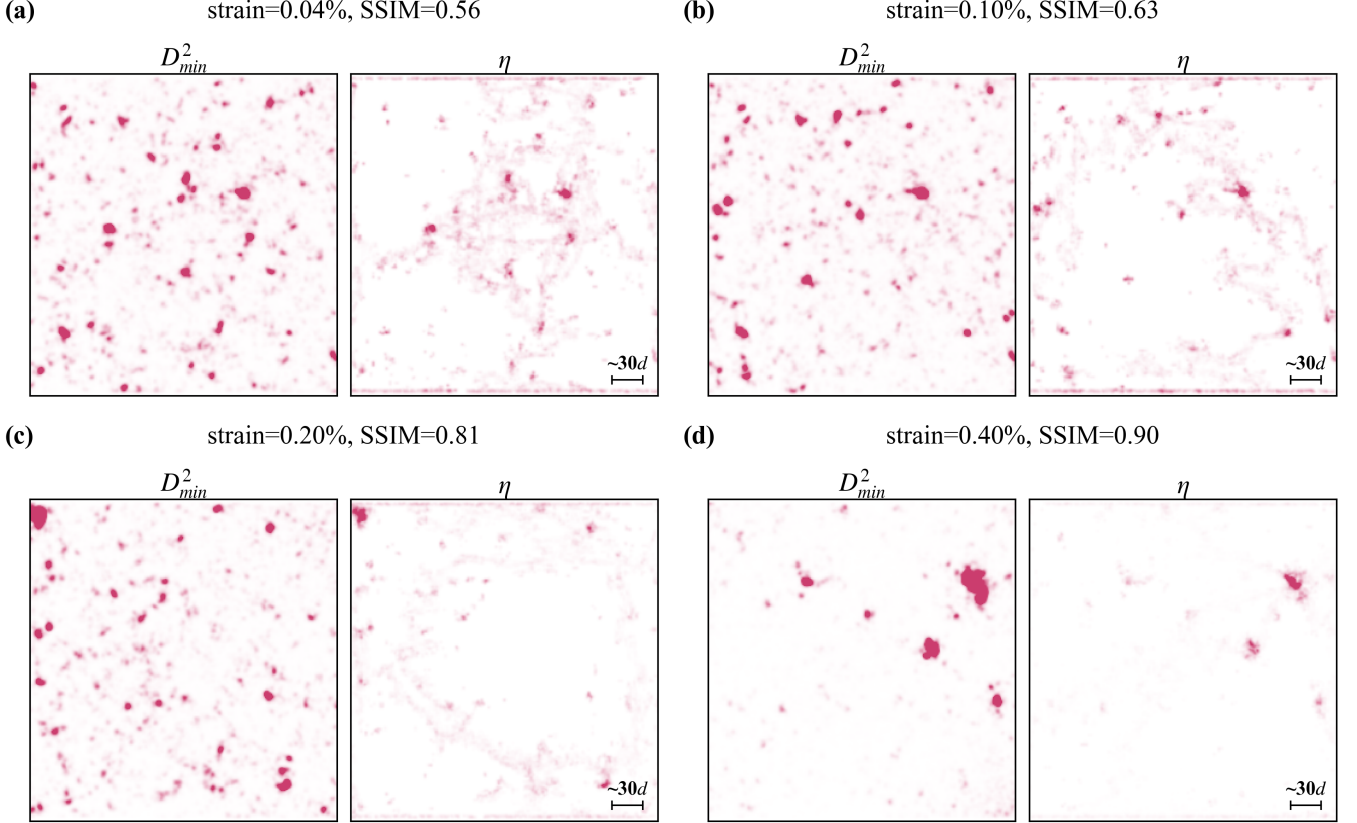


FIG. S10. Comparison between D_{\min}^2 and incompatibility density η at low strain for the 2D Lennard-Jones glass. The corresponding SSIM values are reported on top of each panel.

By contrast, panel (d) shows a slightly larger—yet still small—strain ($\gamma = 0.4\%$), where the SSIM increases substantially. In this case, plastic events become fewer but more pronounced, leading to a much clearer correspondence between the two measures.

A step-by-step comparison is provided in the Supplementary Video `d2min_density.mp4`.

SI8: Demonstration of the robustness of plastic defect structures with respect to grid size, interpolation scheme, and grid positioning

To validate the robustness of our calculations of the density fields, we systematically varied the interpolation grid size, the interpolation scheme, and the relative positioning of the grid used to compute the various fields in the simulated system.

By varying the grid size (Fig. S11), we find that the locations of high density regions remain unchanged across a wide range of resolutions. This demonstrates that our results are not sensitive to the discretization scale, indicating that these regions correspond to intrinsic singular features of the displacement field, whose identification is independent of the specific interpolation grid.

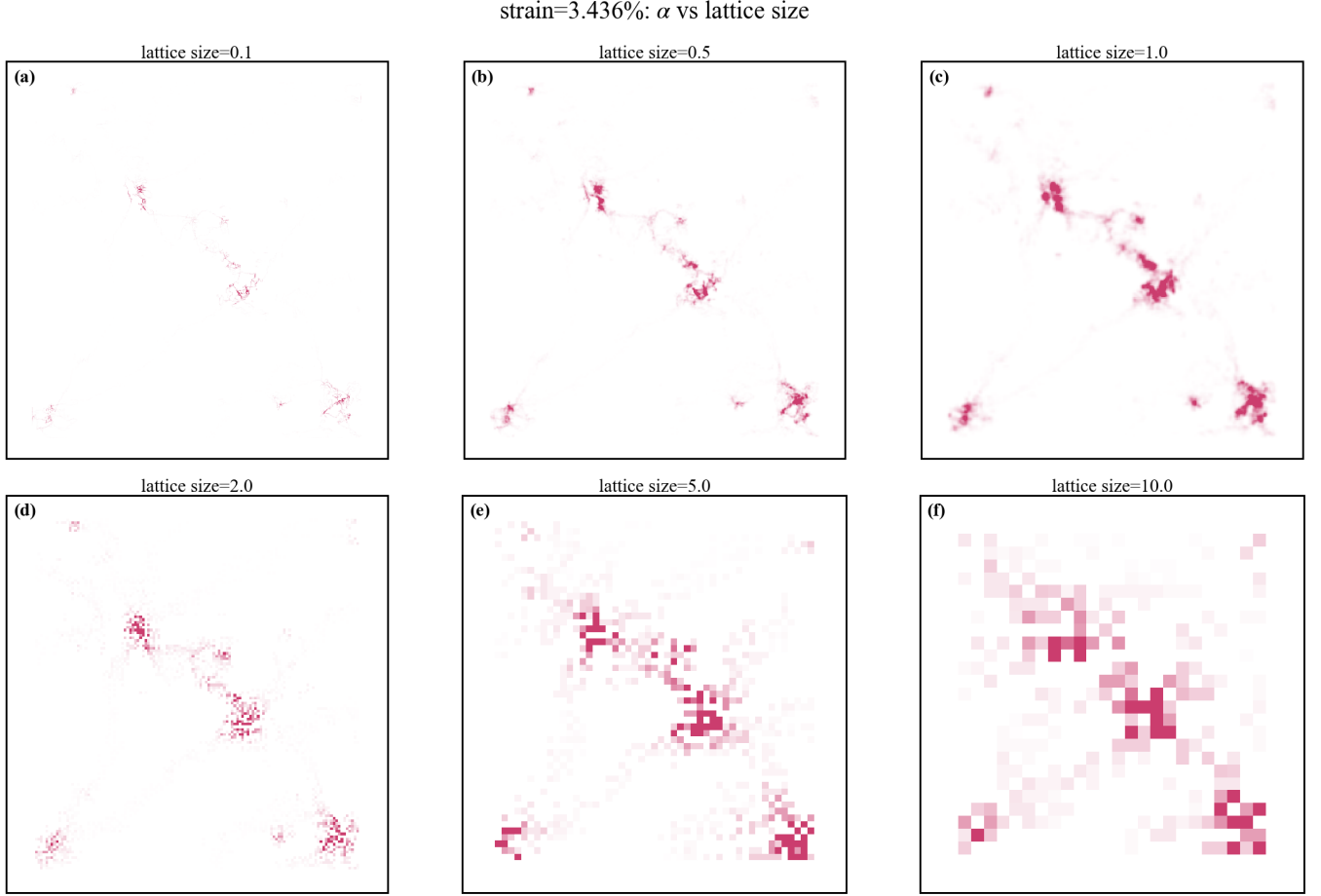


FIG. S11. Dislocation density amplitude $|\tilde{\alpha}(x, y)|$ computed using different grid sizes at $\gamma = 3.4\%$. Panels (a–f) correspond to grid sizes ranging from 0.1 to 10.0, as indicated in each subplot. The color intensity represents the local magnitude of the dislocation density. All fields are normalized to have values in an interval $[0, 1]$.

Furthermore we tested whether the interpolation scheme used to calculate the derivatives of the displacement field affects the results. For this we considered three schemes—linear, cubic, and Gaussian and present the results in Fig. S12. The resulting patterns are nearly identical, indicating that the observed singular structures are not artifacts of the interpolation procedure.

Finally, we examined the effect of shifting the grid relative to the system boundaries (Fig. S13). Specifically, we changed the initial and final positions of the interpolation, thereby effectively shifting the positions of the interpolation grid for different shift values. By excluding different boundary regions and varying the grid offset, we again observe that the locations of high topological density remain invariant. This further confirms that the identified features are intrinsic to the displacement field and not introduced by the interpolation or the alignment of the grid.

SI9: Extended analysis on continuous defect densities in 2D experimental granular systems

In Fig. S14, we provide further examples in which we compare the fields for the dislocation, disclination and incompatibility densities, and D_{\min}^2 for different values of the shear strain γ . The corresponding similarity degree is shown in Fig. (3)(b). For all cases one finds a good correspondence between the spatial structure of the different fields.

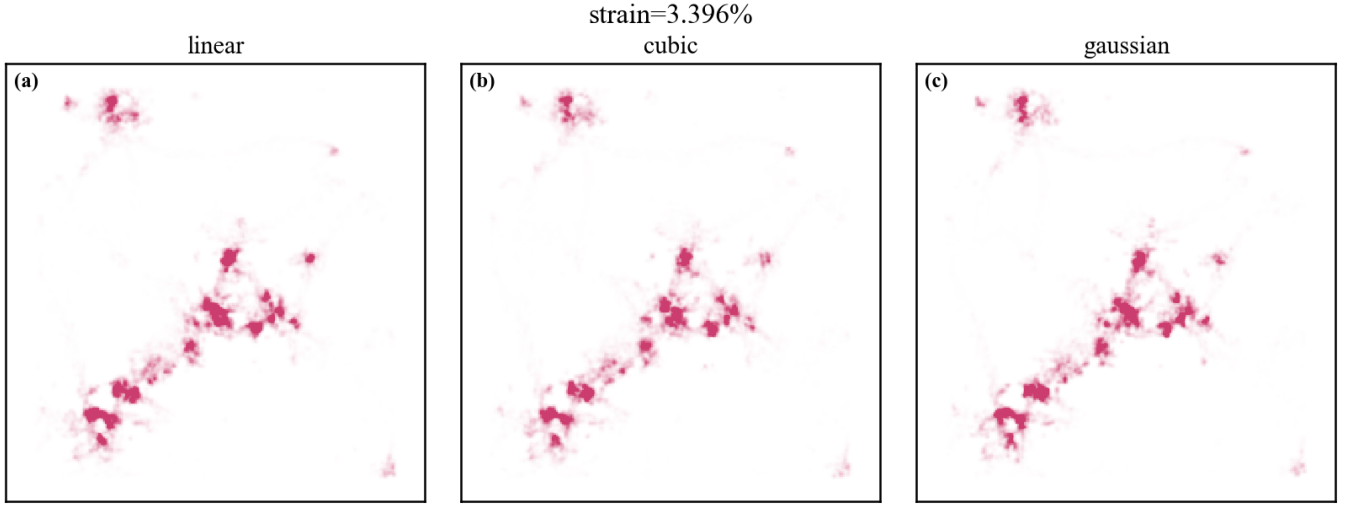


FIG. S12. Dislocation density obtained using (a) linear, (b) cubic, and (c) Gaussian interpolation of the displacement field. Here, $\gamma = 3.4\%$. The color intensity represents the local magnitude of the dislocation density.

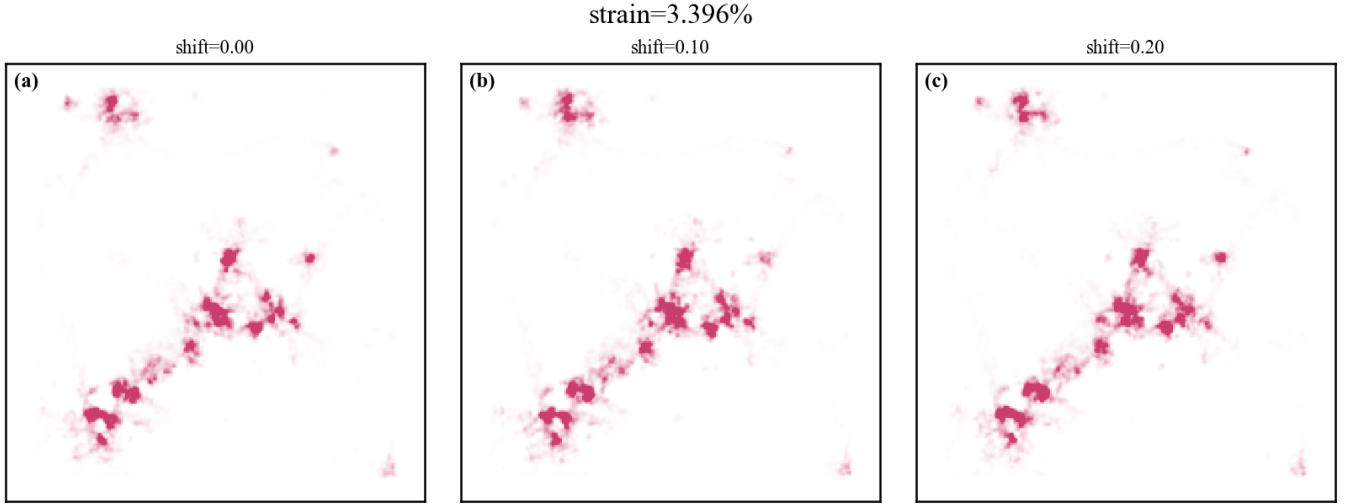


FIG. S13. Effect of shifting the interpolation grid relative to the system boundary. Here, $\gamma = 3.4\%$. The initial offset is 5.0 with additional shifts along the diagonal direction of (a) 0.0, (b) 0.1, and (c) 0.2. The color intensity represents the magnitude of the dislocation density.

SI10: Stability of the similarity analysis against grid size and interpolation scheme

In Figs. S15, we demonstrate the robustness of our similarity analysis with respect to both the grid size and the interpolation scheme. The panels correspond to the 2D experimental data, with the specific parameters and methods indicated in each caption. The qualitative agreement across different choices is clear. Consistently, the SSIM analysis reported in Fig. S16 exhibits the same behavior, and becomes larger when the grid chosen is not too small.

SI11: Defects captured by continuous densities and comparison to vortex-like defects

To clarify the nature of the geometric defects captured by the continuous densities introduced in this work, Fig. S17 presents additional snapshots of the particle displacement field for both the simulated 2D Lennard-Jones system and the experimental 2D granular system. Yellow–orange regions indicate the location of plastic defects, i.e., localized areas where the Nye dislocation density attains large values.

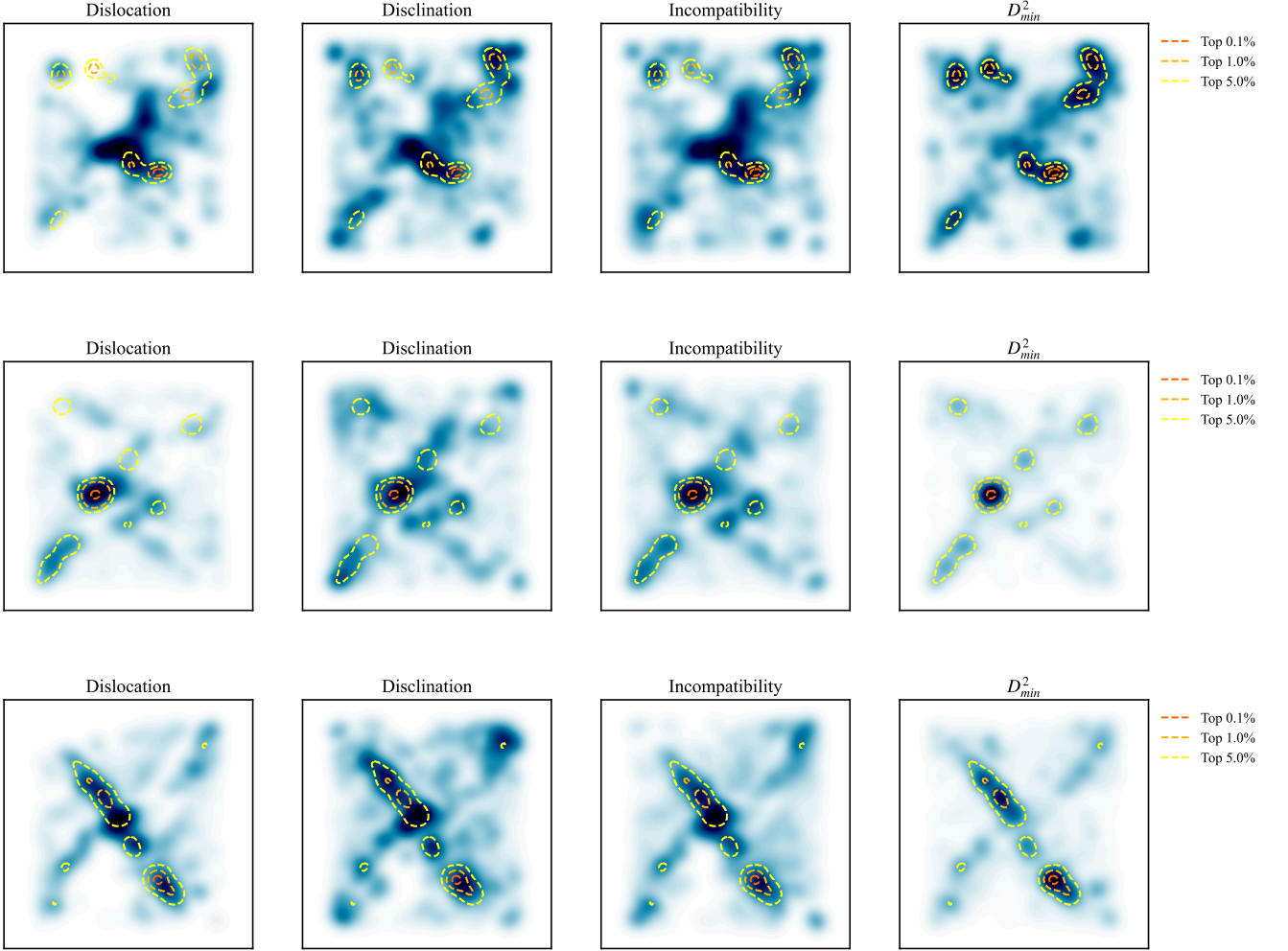


FIG. S14. Heat maps of the dislocation, disclination, and incompatibility densities, together with D_{\min}^2 , for the 2D experimental data. For the dislocation density, we plot the norm of $\vec{\alpha}$. The applied strains are (top) $\gamma = 2.83\%$, (middle) $\gamma = 3.40\%$, and (bottom) $\gamma = 3.96\%$.

For completeness, we also consider topological defects in the phase angle of the displacement field, defined through the winding number

$$w \equiv \frac{1}{2\pi} \oint d\theta, \quad (\text{S6})$$

where θ denotes the local orientation of the displacement vector field. We evaluate w over the smallest available loops within the regular grid and identify regions with $w = +1$ as topological vortices and those with $w = -1$ as anti-vortices.

In Fig. S17, these phase defects are superimposed on the continuous Nye dislocation density for the 2D systems. Anti-vortices and vortices are marked by white crosses and white disks, respectively. We observe a clear correlation between regions of high dislocation density and areas with an elevated local density of vortex-like defects. Notably, all regions with large dislocation density involve at least a vortex dipole, and often more complex configurations composed of defects with alternating sign. In contrast, isolated vortex-like defects with $+1$ winding number rarely produce a noticeable signature in the dislocation density. This suggests that it is the collective accumulation of such defects—rather than their existence as individual entities—that is essential for capturing plastic rearrangements in glasses. Moreover, it highlights the greater significance of -1 defects, $+/-$ dipoles, and more complex clusters compared to isolated $+1$ vortices.

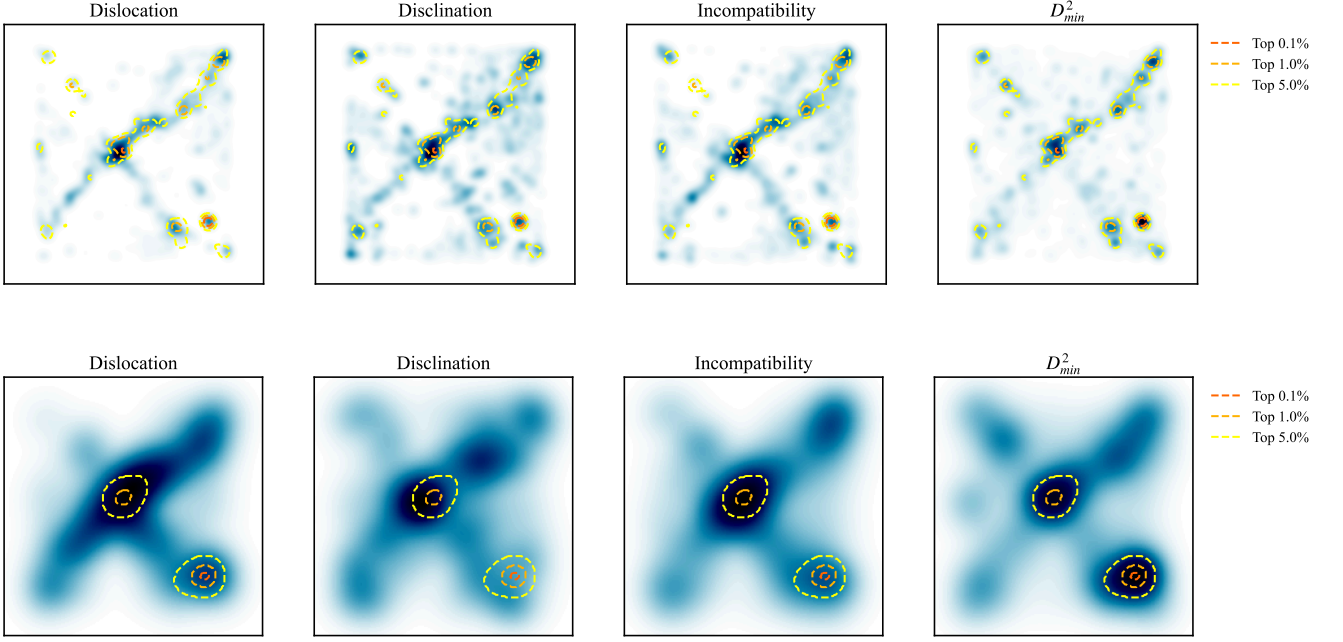


FIG. S15. Influence of the grid size a used for calculating the derivatives on the spatial distribution of the various fields. The system is the 2D experiment. **Top:** Grid size $a = 0.5 d_s$. **Bottom:** Grid size $a = 2.25 d_s$.

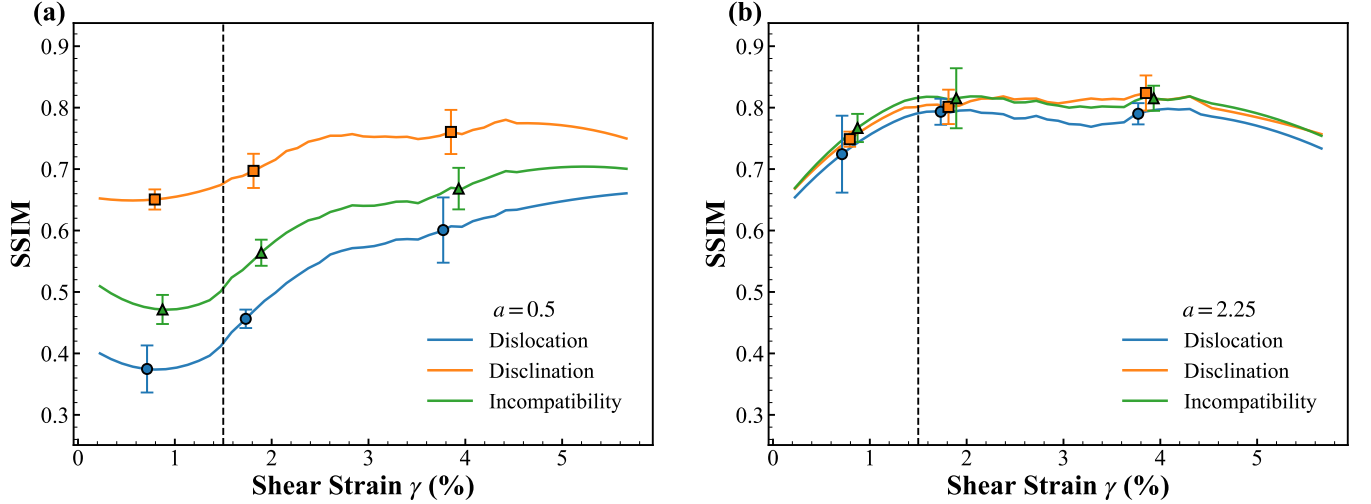


FIG. S16. (a) Linear interpolation for 2D experiment: grid size $a = 0.5 d_s$. (b) Linear interpolation and coarse grain for 2D experiment: grid size $a = 2.25 d_s$.

SI12: Ideal topological defects and their singular contribution to the continuous defect densities

Given the particle trajectories, one can construct a continuous displacement field $u_i(\mathbf{x})$, where $\mathbf{x} = (x, y, z)$ in 3D and $\mathbf{x} = (x, y)$ in 2D. The Burgers vector is then defined as the circulation of the displacement field along a closed loop:

$$b_j(\mathbf{x}) = \oint du_j = \oint \partial_k u_j(\mathbf{x}) dx_k. \quad (\text{S7})$$

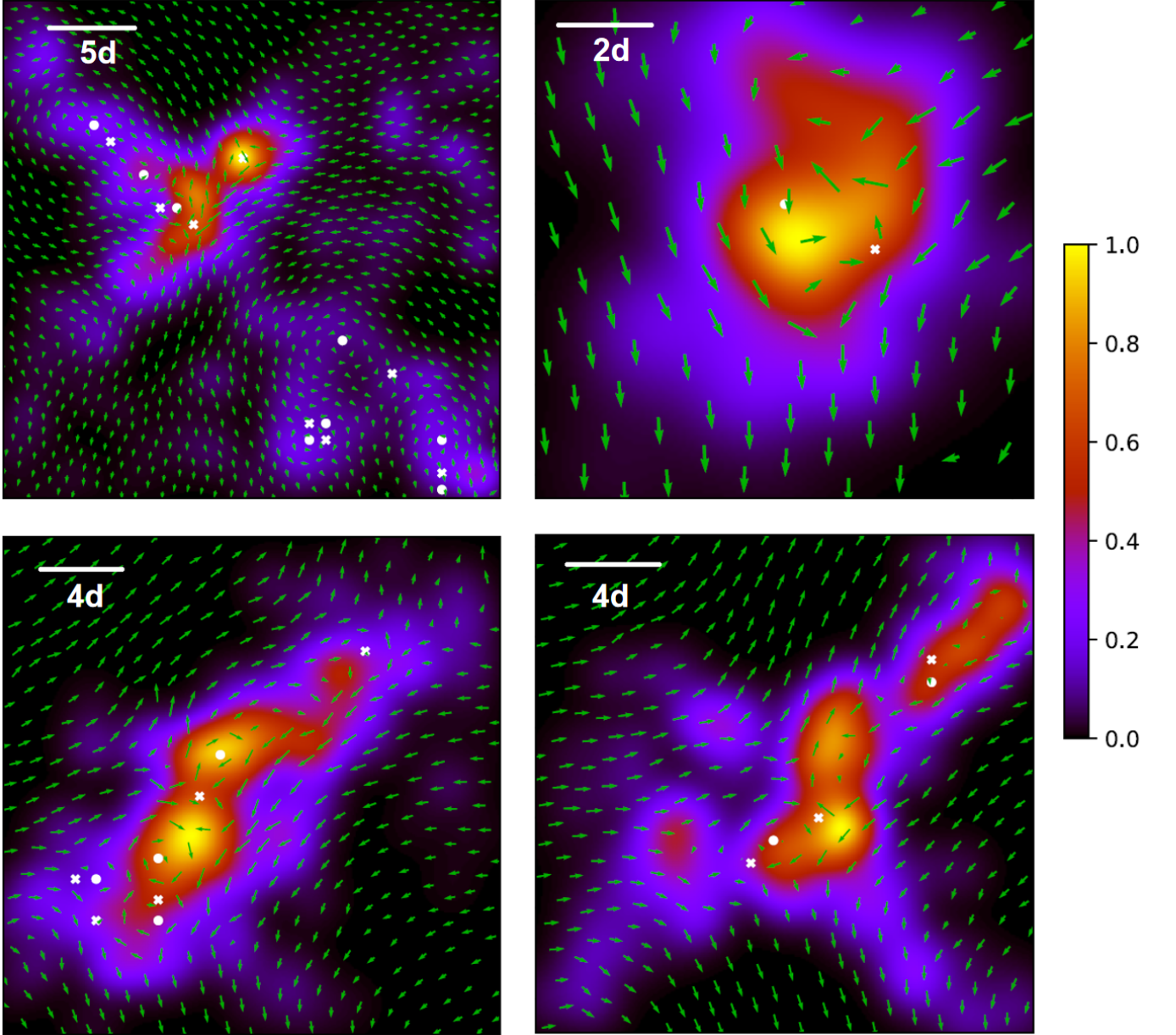


FIG. S17. Snapshots of the two-dimensional particle displacement field, highlighting the geometric nature of the defects captured by the continuous dislocation density (yellow/orange areas). The dislocation density is normalized to its maximum value in each panel. The top-left panel corresponds to the 2D simulated Lennard-Jones glass, while all other panels are for the 2D experimental granular system. White crosses and disks denote vortex-like defects with winding numbers $w = -1$ (anti-vortices) and $w = +1$ (vortices), respectively. In all panels, d indicates the particle diameter.

Applying Stokes' theorem, this can be rewritten as a surface integral:

$$b_j(\mathbf{x}) = \int \epsilon_{ilk} \partial_l \partial_k u_j(\mathbf{x}) dS_i, \quad (\text{S8})$$

which naturally leads to the definition of the Nye tensor,

$$\alpha_{ij}(\mathbf{x}) = \epsilon_{ilk} \partial_l \partial_k u_j(\mathbf{x}), \quad (\text{S9})$$

describing, in crystals, the local density of dislocations.

For a smooth (single-valued and differentiable) displacement field, mixed partial derivatives commute, and therefore $\alpha_{ij}(\mathbf{x}) = 0$.

In two dimensions, the only nonzero components of the Nye tensor are

$$\alpha_{zi} = \epsilon_{zmn} \partial_m \partial_n u_i = (\partial_x \partial_y - \partial_y \partial_x) u_i = [\partial_x, \partial_y] u_i, \quad (\text{S10})$$

which explicitly measures the non-commutativity of derivatives and thus the local defect content.

Let us consider the canonical displacement field of a 2D dislocation with Burgers vector along x ,

$$u_x = \frac{b}{2\pi} \arctan\left(\frac{y}{x}\right) + u_x^{\text{reg}}, \quad u_y = u_y^{\text{reg}}, \quad (\text{S11})$$

where u^{reg} denotes a smooth (regular) contribution. Since the Nye tensor only probes singular terms, the smooth part does not contribute and can be ignored.

It follows immediately that

$$\alpha_{zy} = [\partial_x, \partial_y] u_y = 0, \quad (\text{S12})$$

and we only need to analyze the singular part of u_x .

Away from the origin $(x, y) \neq (0, 0)$, derivatives commute and one finds

$$\partial_x u_x = -\frac{b}{2\pi} \frac{y}{x^2 + y^2}. \quad (\text{S13})$$

However, the function $\arctan(y/x)$ is multivalued and exhibits a branch cut (along, e.g., the negative x -axis), which generates a singular contribution. Taking this into account in the sense of distributions, one obtains

$$[\partial_x, \partial_y] u_x = \partial_x \partial_y u_x - \partial_y \partial_x u_x = b \delta(x) \delta(y). \quad (\text{S14})$$

Therefore,

$$\alpha_{zx}(\mathbf{x}) = b \delta(x) \delta(y), \quad (\text{S15})$$

showing that the Nye tensor is localized at a point and corresponds to a topological defect with Burgers vector b .

To consider the case of a disclination, we introduce the local rotation (vorticity) as

$$\omega_i(\mathbf{x}) = \frac{1}{2} \epsilon_{ijk} \partial_j u_k(\mathbf{x}). \quad (\text{S16})$$

The antisymmetric quantity $\omega_i(\mathbf{x})$ captures local rigid-body rotations.

In direct analogy with the Burgers vector for dislocations, one can define defect densities associated with the rotation field. These are described by the Frank tensor, which quantifies in crystals the density of disclinations.

A minimal analytical displacement field describing a combined dislocation (with Burgers vector \mathbf{b}) and disclination (with strength d_{xy}) is

$$\begin{aligned} u_x(\mathbf{x}) &= \frac{b_x + d_{xy}y}{2\pi} \arctan\left(\frac{y}{x}\right) + \frac{-b_y - d_{xy}x}{4\pi} \ln(x^2 + y^2), \\ u_y(\mathbf{x}) &= \frac{b_y - d_{xy}x}{2\pi} \arctan\left(\frac{y}{x}\right) + \frac{b_x - d_{xy}y}{4\pi} \ln(x^2 + y^2). \end{aligned} \quad (\text{S17})$$

From this, the scalar vorticity (in 2D) reads

$$\omega(\mathbf{x}) = \frac{1}{2} (\partial_x u_y - \partial_y u_x) = -\frac{d_{xy}}{2\pi} \arctan\left(\frac{y}{x}\right) + \frac{1}{4\pi} \frac{yb_y - xb_x}{x^2 + y^2}. \quad (\text{S18})$$

Both the displacement field and the rotation contain the multivalued function $\arctan(y/x)$, which introduces a branch cut. As a consequence, derivatives do not commute in the distributional sense, leading to nonzero defect densities. Specifically:

- The non-commutativity of derivatives acting on $u_i(\mathbf{x})$ gives a nonzero Nye tensor, corresponding to a dislocation localized at the origin.
- The non-commutativity of derivatives acting on $\omega(\mathbf{x})$ gives a nonzero Frank tensor, corresponding to a disclination.